JCTC Journal of Chemical Theory and Computation

Article

Cite This: J. Chem. Theory Comput. XXXX, XXX, XXX−XXX

pubs.acs.org/JCTC

Probing Molecular Chirality by Orbital-Angular-Momentum-Carrying X-ray Pulses

Lyuzhou Ye,*[,†] Jérémy R. Rouxel,[‡,§] Shahaf Asban,[†] Benedikt Rösner,[§] and Shaul Mukamel*[,†]

[†]Department of Chemistry and Department of Physics and Astronomy, University of California, Irvine, California 92697, United States

[‡]Laboratory of Ultrafast Spectroscopy, École Polytechnique Fédérale de Lausanne, Lausanne CH-1015, Switzerland

[§]Paul Scherrer Institut, Villigen-PSI 5232, Switzerland

Supporting Information

ABSTRACT: A twisted X-ray beam with orbital angular momentum is employed in a theoretical study to probe molecular chirality. A nonlocal response description of the matter-field coupling is adopted to account for the field short wavelength and the structured spatial profile. We use the minimal-coupling Hamiltonian, which implicitly takes into account the multipole contributions to all orders. The combined interactions of the spin and orbital angular momentum of the X-ray beam give rise to circular-helical dichroism signals, which are stronger than ordinary circular dichroism signals, and may serve as a useful tool for the study of molecular chirality in the X-ray regime.

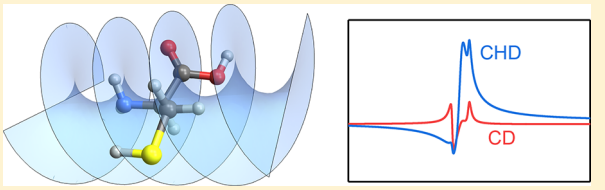

1. INTRODUCTION

Chirality is relevant to many processes including catalysis,[1−3] drug design,[4,5] and biochemistry.[6−9] Circular dichroism (CD) signals given by the difference between absorption of left (LCP) and right (RCP) circularly polarized light are widely used to discriminate enantiomers[10−12] and remain the most common technique to study chiral molecules.[13,14] The CD signal is generally weak as compared to absorption, less than a percent, because interaction with a magnetic field through a magnetic dipole is required to obtain a pseudoscalar observable. This chiral observable depends on the scalar product of the field polarization, that is, its spin degree of freedom, and a scalar product of the electric and magnetic transition dipoles matrix elements, known as the rotatory strength. As such, CD utilizes the spin angular momentum (SAM) of light that can take values $s = \pm 1$. Methods for enhancing weak CD signals have been proposed.[15] First, it is possible to employ shorter wavelengths where the multipolar expansion can lead to a more favorable chiral contribution. Second, techniques other than CD can offer a lower background (e.g., Raman optical activity) or are allowed in the electric dipole approximation (e.g., photoelectron CD), making them stronger.

In this Article, we study the interaction of orbital angular momentum (OAM) of light with chiral matter. Examples of beams carrying a well-defined OAM[16−18] are the Laguerre−Gauss or the Hypergeometric−Gaussian modes. In both cases, the OAM gives a twist to the phase that then rotates along the propagation axis, in a screw-like manner. Such beams have been used for optical manipulation,[19−22] quantum imaging,[23−26] and quantum information processing.[27−32] OAM-carrying light beams have been generated in the extreme-ultraviolet[33−37] and in the X-ray[38−46] regimes.

The simplest chirality-specific technique that can be envisioned with OAM beams is helical dichroism (HD): the differential absorption of beams carrying a $+l$ and a $-l$ angular momentum.[47] We show how such signals can be described and simulated by taking into account the complete spatial variation of the incoming beam. To this end, we start with the minimal coupling Hamiltonian, which avoids the multipolar expansion,[48] and implicitly includes all multipoles. Previous theoretical[49,50] and experimental[51−53] studies have confirmed that no chiral OAM effects are observed by only taking into account the electric dipole and magnetic dipole transition moments. A recent experiment has shown that twisted light can interact with the electric quadrupoles of adsorbed chiral molecules in plasmonic nanoparticle aggregates.[47] HD could then resolve enantiomers for various values of the OAM. Forbes et al. have shown that chiral effects can be probed by twisted light in systems possessing orientational order by using the quadrupole interaction.[48] All of these studies have employed the multipolar interaction Hamiltonian, only retaining the lower-order multipoles, but did not rule out the possibilities that higher-order multipoles may contribute to the chiral signals. This issue will be investigated here.

In section 2, we present the minimal-coupling Hamiltonian for the radiation−matter interaction. Because of the short wavelength and the structured spatial profile of the twisted X-ray beam, the light field variation across the molecule is non-negligible, and the nonlocal response description of the matter−field couplings[54,55] is called for. We also discuss the various configurations of differential absorption involving SAM, OAM, or both. The combined action of the SAM and

Received: April 8, 2019
Published: May 24, 2019

DOI: 10.1021/acs.jctc.9b00346
J. Chem. Theory Comput. XXXX, XXX, XXX−XXX

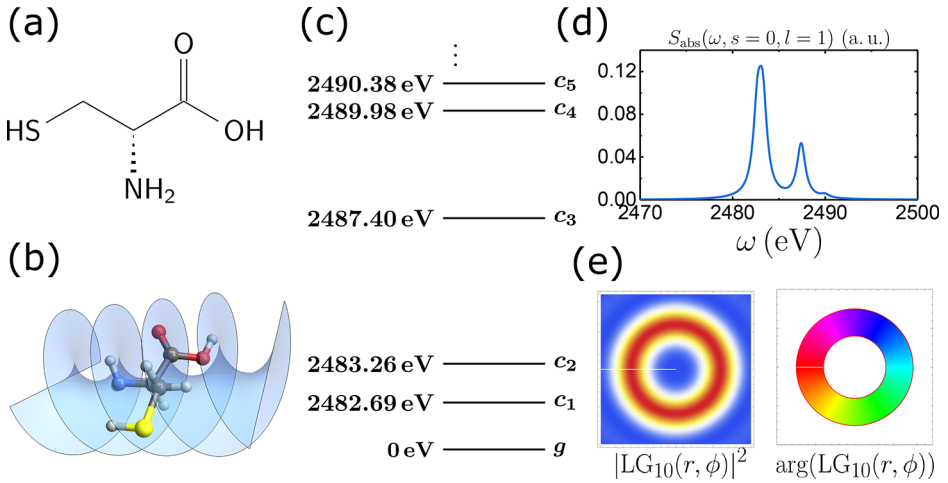

Figure 1. (a) Chemical structure of cysteine. (b) Spatial variation of the LG beam. (c) Energy levels of the ground (g) and core-excited (c_1,c_2,...) states calculated from ab initio quantum chemistry. (d) X-ray linear absorption from the states displayed in (c). A broadening $\Gamma = 0.54$ eV has been included. (e) Intensity (left) and phase (right) profile of the Laguerre−Gauss beam $LG_{10}(r,\phi,z = 0)$; see eq 6.

OAM of the light beam gives rise to circular-helical dichroism (CHD) signals. We show that these can be stronger than their CD counterparts. In section 3, we use ab initio quantum chemistry calculation to simulate the action of a twisted X-ray beam on the amino acid cysteine at the sulfur K-edge (2.48 keV) to probe its chirality. Cysteine is an archetypical chiral molecule that is small enough to allow high level ab initio calculations.

2. HELICAL DICHROISM IN THE MINIMAL COUPLING HAMILTONIAN

To calculate the CD and HD signals, we start with the minimal-coupling field−matter interaction:[54,55]

$$H_{\mathrm{int}} = -\int \mathrm{d}\boldsymbol{r}\left[\hat{\boldsymbol{j}}(\boldsymbol{r}) - \frac{e}{2mc}\hat{\sigma}(\boldsymbol{r})\boldsymbol{A}(\boldsymbol{r})\right]\cdot\boldsymbol{A}(\boldsymbol{r}) \tag{1}$$

where $\boldsymbol{A}(\boldsymbol{r})$ is the electromagnetic vector potential.

$$\hat{\boldsymbol{j}}(\boldsymbol{r}) = \frac{e\hbar}{2mi}\{\psi^{\dagger}(\boldsymbol{r})\nabla\psi(\boldsymbol{r}) - [\nabla\psi^{\dagger}(\boldsymbol{r})]\psi(\boldsymbol{r})\} \tag{2}$$

is the bare current density operator, and

$$\hat{\sigma}(\boldsymbol{r}) = e\psi^{\dagger}(\boldsymbol{r})\psi(\boldsymbol{r}) \tag{3}$$

is the charge density operator, with $\psi^{\dagger}(\boldsymbol{r})$ and $\psi(\boldsymbol{r})$ being the electron field creation and annihilation operators at position $\boldsymbol{r}$. The charge density contribution dominates off-resonant signals, while resonant signals are dominated by the $\boldsymbol{j}\cdot\boldsymbol{A}$ term. In the following, we focus on the resonant absorption at the sulfur K-edge and neglect the charge density term. The linear absorption is given by[54,56]

$$S_{\mathrm{abs}}(t, \pm s, \pm l) = -\frac{2}{\hbar^2}\mathrm{Im}\sum_c \int \mathrm{d}\boldsymbol{r}\,\mathrm{d}\boldsymbol{r}'\boldsymbol{A}^{*}(\boldsymbol{r}, \pm s, \pm l)\boldsymbol{A}(\boldsymbol{r}', \pm s, \pm l) \times [\boldsymbol{j}_{gc}(\boldsymbol{r})\mathrm{e}^{-i\omega_{gc}t-\Gamma_{cg}t}\boldsymbol{j}_{cg}(\boldsymbol{r}') - \boldsymbol{j}_{cg}(\boldsymbol{r})\mathrm{e}^{-i\omega_{cg}t-\Gamma_{gc}t}\boldsymbol{j}_{gc}(\boldsymbol{r}')] \tag{4}$$

Here, s and l denote the spin and orbital angular momentum, respectively. Derivation of eq 4 is given in section S1 of the Supporting Information. In the frequency-domain, we assume monochromatic beams, and eq 4 reads

$$S_{\mathrm{abs}}(\omega, \pm s, \pm l) = -\frac{2}{\hbar^2}\mathrm{Im}\sum_c \int \mathrm{d}\boldsymbol{r}\,\mathrm{d}\boldsymbol{r}' \left[\frac{\langle \boldsymbol{j}_{gc}(\boldsymbol{r})\cdot\boldsymbol{A}^{*}(\boldsymbol{r}, \pm s, \pm l)\boldsymbol{j}_{cg}(\boldsymbol{r}')\cdot\boldsymbol{A}(\boldsymbol{r}', \pm s, \pm l)\rangle_{\Omega}}{\omega - \omega_{gc} + i\Gamma_{gc}} - \frac{\langle \boldsymbol{j}_{cg}(\boldsymbol{r})\cdot\boldsymbol{A}^{*}(\boldsymbol{r}, \pm s, \pm l)\boldsymbol{j}_{gc}(\boldsymbol{r}')\cdot\boldsymbol{A}(\boldsymbol{r}', \pm s, \pm l)\rangle_{\Omega}}{\omega - \omega_{cg} + i\Gamma_{cg}}\right] \tag{5}$$

where $\langle\cdots\rangle_{\Omega}$ denotes rotational averaging of the current density tensor.

We assume that the transverse spatial profile of the vector potential $\boldsymbol{A}$ is given by a Laguerre−Gaussian (LG) mode, which in cylindrical coordinates (r,ϕ,z) takes the form:[16,17]

$$\mathrm{LG}_{lp}(r, \phi, z) = \sqrt{\frac{2p!}{\pi(p + |l|)!}}\frac{w_0}{w(z)}\exp\left(-\frac{r^2}{w^2(z)}\right)\left(\frac{\sqrt{2}r}{w(z)}\right)^{|l|}\exp\left(-ik_0\frac{r^2}{2R(z)}\right)\times L_p^{|l|}\left[\frac{2r^2}{w^2(z)}\right]\mathrm{e}^{i\phi_{lp}(z)}\mathrm{e}^{il\phi} \tag{6}$$

Here, $l \in \mathbb{Z}$ is the OAM value and describes the azimuthal variation of the phase front and $p \in \mathbb{N}_0$ indicates the number of radial nodes. The transverse spatial extent of the wave is described by the beam width $w(z) = w_0\sqrt{1 + z^2/z_{\mathrm{R}}^2}$ with w_0 being the beam waist. The radius of curvature is $R(z) = z + z_{\mathrm{R}}^2/z$ with the Rayleigh length $z_{\mathrm{R}} = \pi w_0^2/\lambda$. The Gouy phase is given by $\phi_{lp}(z) = (2p + |l| + 1)\arctan(z/z_{\mathrm{R}})$. $L_p^{|l|}$ represents the generalized Laguerre polynomials.

The CD signal is defined as the difference between the absorption of LCP and RCP pulses normalized by their average:

$$S_{\mathrm{CD}}(\omega) = \frac{2[S_{\mathrm{abs}}(\omega, s = 1, l = 0) - S_{\mathrm{abs}}(\omega, s = -1, l = 0)]}{S_{\mathrm{abs}}(\omega, s = 1, l = 0) + S_{\mathrm{abs}}(\omega, s = -1, l = 0)} \tag{7}$$

The HD signal is similarly defined as the normalized difference between the absorption of left-handed $(+l)$ and right-handed $(-l)$ X-ray pulses with linear polarization $(s = 0)$:[47]

DOI: 10.1021/acs.jctc.9b00346
J. Chem. Theory Comput. XXXX, XXX, XXX−XXX

$$S_{\mathrm{HD}}(\omega, l) = \frac{2[S_{\mathrm{abs}}(\omega, s=0, l) - S_{\mathrm{abs}}(\omega, s=0, -l)]}{S_{\mathrm{abs}}(\omega, s=0, l) + S_{\mathrm{abs}}(\omega, s=0, -l)} \tag{8}$$

Finally, for light carrying both SAM and OAM, we define the circular-helical dichroism signal:

$$S_{\mathrm{CHD}}(\omega, s, l) = \frac{2[S_{\mathrm{abs}}(\omega, s, l) - S_{\mathrm{abs}}(\omega, -s, -l)]}{S_{\mathrm{abs}}(\omega, s, l) + S_{\mathrm{abs}}(\omega, -s, -l)} \tag{9}$$

S_{CHD} reduces to S_{CD} (eq 7) for $l = 0$ and $s = 1$, and to S_{HD} (eq 8) for $s = 0$. Other possible types of dichroism signals can be found in ref 57.

The HD signal is sensitive to molecular chirality, and vanishes for achiral molecules. To show that, we note that the spatial profile of the vector potential transforms under parity inversion as $\mathcal{P}\boldsymbol{A}(\boldsymbol{r}, -l) = \boldsymbol{A}(-\boldsymbol{r}, -l) = \boldsymbol{A}(\boldsymbol{r}, l)$. We then get

$$S_{\mathrm{abs}}(\omega, +l) - S_{\mathrm{abs}}(\omega, -l) \propto \int \mathrm{d}\boldsymbol{r}\, \mathrm{d}\boldsymbol{r}' \boldsymbol{A}^*(\boldsymbol{r}, l)\boldsymbol{A}(\boldsymbol{r}', l) \left[\langle \boldsymbol{j}_{gc}(\boldsymbol{r})\boldsymbol{j}_{cg}(\boldsymbol{r}')\rangle_\Omega - \langle \boldsymbol{j}_{gc}(-\boldsymbol{r})\boldsymbol{j}_{cg}(-\boldsymbol{r}')\rangle_\Omega\right] \tag{10}$$

$\langle \boldsymbol{j}_{gc}(\boldsymbol{r})\boldsymbol{j}_{cg}(\boldsymbol{r}')\rangle_\Omega - \langle \boldsymbol{j}_{gc}(-\boldsymbol{r})\boldsymbol{j}_{cg}(-\boldsymbol{r}')\rangle_\Omega$ vanishes for achiral mol-

$= (1 - \mathcal{P})\langle \boldsymbol{j}_{gc}(\boldsymbol{r})\boldsymbol{j}_{cg}(\boldsymbol{r}')\rangle_\Omega$

ecules but does not for chiral molecules.

3. CHIRAL RESPONSE AT THE SULFUR K-EDGE OF CYSTEINE

We have simulated the HD, CD, and CHD signals of cysteine at the sulfur K-edge (see Figure 1a and b). The core excited states are calculated by using the MOLPRO program[58] with the second-order Douglas−Kroll−Hess Hamiltonian.[59,60] The sulfur 1s orbital was rotated into the active space, and restricted to single occupancy. The geometry was optimized at the Hartree−Fock/cc-pVDZ[61] level of theory. The sulfur 1s core excited states were then obtained by the restricted active space (RASSCF) method at the RASSCF(8/7)/cc-pVDZ level of theory.[61−64] The resulting manifold of states is displayed in Figure 1c. The first core excited state is at $\omega_{c1,g}$ = 2482.7 eV in agreement with experiment.[65] The linear absorption is displayed in Figure 1d using a Lorentzian broadening of 0.54 eV. Rotational averaging in the minimal coupling representation is complicated because we use vector fields rather than a simple vectors. To address this challenge numerically, we have expanded the Laguerre−Gauss beams in Hermite polynomials. The integrand of the spatial integrals then reduces to a product of Hermite polynomials and the rotated Gaussian-type orbital basis elements, which can be calculated analytically. Details are given in the Supporting Information. Note that the position of the molecule within the beam is crucial. The molecule is sensitive to the phase rotation of the LG beam, that is, its angular momentum, only in close vicinity of the singularity along the propagation axis.

We first consider molecules located at the singularity and then discuss the effect of the displacement from this axis. The absorption signals were calculated using eq 5, and the HD, CD, and CHD signals for various SAM and OAM values (s,l) were obtained using eqs 7−9. We have used the following parameters for the LG beam: w_0 = 60 nm, z_R = 22.6 μm, and p = 0. In section S4 of the Supporting Information, we repeat the analysis for a tighter focus, w_0 = 15 nm, corresponding to the current available limit.[66,67] Such values for the beam waist correspond to a degree of focusing achievable with current Fresnel zoneplates manufacturing capabilities.[66−68] In the Supporting Information, we also consider a 15 nm beam waist, close to the state of the art. This tight focus increases the cross-section of HD signals. Beams carrying an angular momentum have in general a ring-shape intensity node in the center of the beam. A tight focus is preferable to ensure that the molecule is located in a region where the beam intensity does not vanish and where the phase gradient exhibits a complete phase rotation. Moreover, if the focus region is large, most molecules contributing to the signal are located away from the singularity and thus experience a phase gradient rather than the complete twist. Thus, they contribute to a more intense absorption background while the HD signal becomes comparatively weaker.

Figure 2 depicts the rotationally averaged CD, HD, and CHD signals (eqs 7−9) for various values of l and s keeping

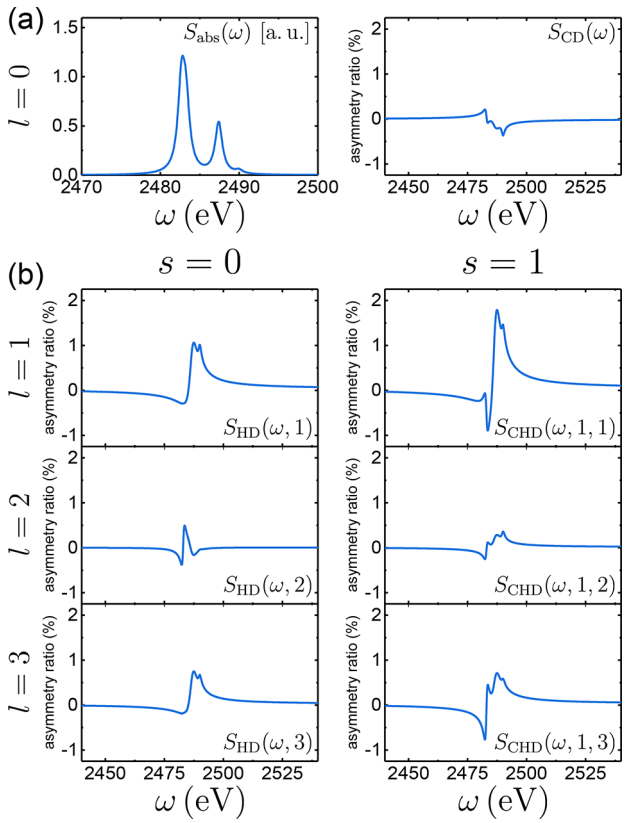

Figure 2. (a) Simulated linear absorption (left), eq 5, and CD (right), eq 7, signals at the S K-edge of cysteine using the nonlocal response. (b) Simulated HD (left column) and CHD (right column) signals, eqs 8 and 9, for various values of l and s. The molecule is placed at the center of the beam.

the molecule at the center of the beam. The signal is dominated by ground to the core excited-state transitions and by transition from the first three excited states (see Figure 1c). In the right panel of Figure 2a, the CD signal shows a 0.2% to −0.3% absorption asymmetry ratio, eq 7. This indicates that the chiral contribution to the absorption signal is weak, which is typical for CD signals. Panels with s = 0 and l = 1,2,3 in Figure 2b show that the HD signals are stronger than the CD signal and have a higher maximum asymmetry ratio up to 1%, eq 8 for l = 1. The s = 1 and l = 1,2,3 panels in Figure 2b

DOI: 10.1021/acs.jctc.9b00346
J. Chem. Theory Comput. XXXX, XXX, XXX−XXX

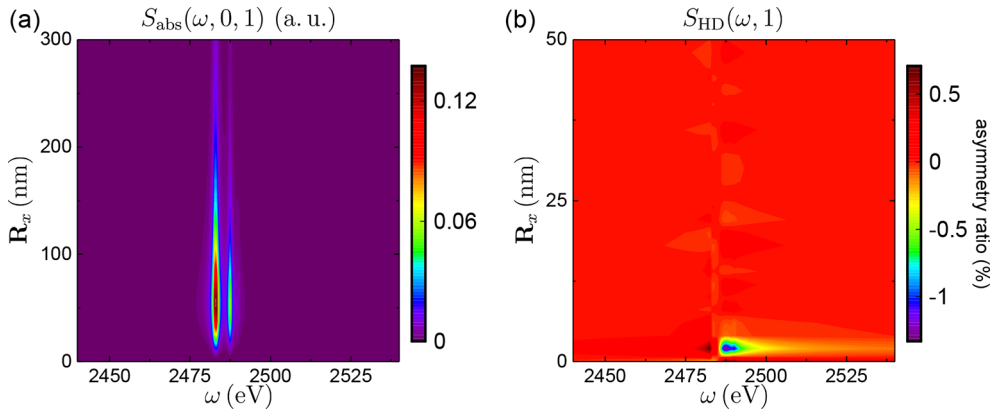

Figure 3. (a) Linear absorption $S_{abs}(\omega,s = 0,l = 1)$ and (b) HD $S_{HD}(\omega,l = 1)$ signal variations with the linear displacement $\boldsymbol{R}_x$ of the molecule from the beam singularity. The beam focus is $w_0 = 60$ nm. The main contribution to the HD signal comes from molecules near the beam propagation axis, close to the phase singularity. This volume also corresponds to the location where the beam intensity is weak, as can be seen in (a).

demonstrate that the combination of SAM and OAM can enhance the asymmetry ratio.

We next examine the signal variation as the molecule is moved away from the focus of the beam. For molecules in solution, the signal involves both rotational and translational averaging over the molecular positions within the beam. Figure 3a depicts the linear absorption signals S_{abs} in the $(\boldsymbol{R}_x,\omega)$ domain for the linearly polarized ($s = 0$) LG beam with $l = 1$, where $\boldsymbol{R}_x$ is the distance between the molecule and z-axis. We have assumed that the X-ray beam propagates along z, and the molecule gets displaced along x. Figure 3a shows that S_{abs} is weak near the focus, and then increases according to the ring shape of the incoming beam intensity (see Figure 1e). The LG beam intensity has a maximum at $R_{max} = \sqrt{x^2 + y^2} = w_0\sqrt{l/2} \approx 42$ nm for $w_0 = 60$ nm and $l = 1$, which results in the maximum of S_{abs} in Figure 3a. Because we assumed $p = 0$, only one concentric ring is observed in the intensity plot, Figure 1e. The beam intensity weakens for $\boldsymbol{R}_x > R_{max}$, and thus the absorption signal S_{abs} gets weaker. The HD signal, Figure 3b, is significant only near $\boldsymbol{R}_x = 0$, and weakens rapidly with increasing $\boldsymbol{R}_x$ as well.

Figure 4 depicts the translationally and rotationally averaged signals for various values of s and l. In Figure 4a, we show CD signals calculated both using the multipolar expansion (truncated at the magnetic dipole) and the minimal coupling Hamiltonian. For the latter, the rotational and translational averaging are done numerically, as described in section S3 of the Supporting Information. Comparing it with the CD signal, the magnetic dipole approximation gives a qualitatively similar result, because it does not fully capture the spatial variation of the X-ray beam. In Figure 4b, we show the HD and CHD signals. The HD signals in the left panels with $s = 0$ are weaker than the CD signal in the top-right panel. This can be rationalized as follows: when the beam does not carry a SAM, the only contribution to the HD signals originates near the singularity as can be seen in Figure 3. The rest of the beam profile gives an intense linear absorption background, because most molecules are located away from the beam focus. The asymmetry then becomes weak due to the large absorption term in the denominator of eq 8. When both SAM and OAM are included, a standard CD interaction occurs also far from the beam, and the OAM acts as an enhancer of this near the focus. Finally, it is worth noting that the strongest HD signal is found for $l = 1$ and the weakest is for $l = 2$, while the strongest

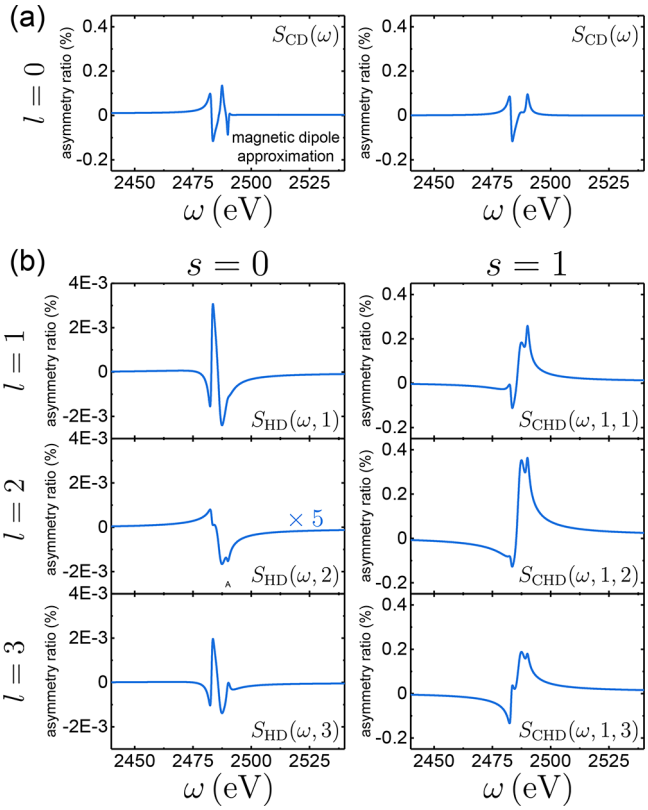

Figure 4. Translationally and rotationally averaged CD, HD, and CHD asymmetry ratios (eqs 7–9) at the S K-edge of cysteine for various values of l and s. (a) Simulated CD signals in the magnetic dipole approximation (left) and minimal coupling (right), respectively. (b) Simulated HD (left column) and CHD (right column) signals.

of the CHD signals is for $l = 2$. Because the translationally averaged CD signal is much stronger than the HD signals, when the SAM is combined with the OAM to produce the CHD signals, it will increase more the asymmetry ratio of the weakest HD signal with $l = 2$. Because the size of the cysteine molecule is much smaller than the beam waist, the CHD signals are generally 2 times stronger than the CD signal. We expect a greater enhancement of the CHD signals if the size of chiral molecule is comparable to or larger than the beam waist.

DOI: 10.1021/acs.jctc.9b00346
J. Chem. Theory Comput. XXXX, XXX, XXX−XXX

4. CONCLUSIONS

Helical dichroism offers a novel probe of molecular chirality, which utilizes the OAM of light rather than its SAM. Unlike the SAM that can take only two values, which represent left and right circular polarization, the OAM can take any integer values and thus offers a higher degree of experimental control.

Previous studies by Andrews et al.[48] had proposed that the OAM interacts with molecules through a quadrupolar coupling. Expansion in multipoles is convenient for carrying out rotational averaging analytically but does not capture the full spatial structure of the beam. Electric multipoles interact with derivatives of the electromagnetic field at the singularity, which vanish for LG beams. To circumvent these difficulties, we have employed the minimal-coupling Hamiltonian, avoiding multipoles altogether. Our approach takes into account the full spatial profile of the incoming beam, that is, its helical structure.

Simulated CD, HD, and CHD signals for cysteine at the sulfur K-edge show that the observed asymmetry ratio of the HD signal is the largest for $l = 1$. Moreover, this ratio can be maximized when the OAM is utilized in conjunction with the SAM and leads to signals that are larger than standard CD. Thus, we have also introduced more general CHD signals that involve both OAM and SAM of light.

In the main text, we have discussed the case of moderately tight focusing $w_0 = 60$ nm. The Supporting Information shows that a tighter 15 nm focus does not lead to large changes in the value of the asymmetry ratio. Indeed, the absorption background is reduced away from the singularity, but the HD signal itself is more narrow too. An interesting case for future study would be to consider chiral objects of the same size as or larger than the beam waist.

The availability of vortex beams with X-ray sources at synchrotrons and XFEL make the proposed experiments feasible with current technology.[38−46] So far, the effect has only been observed with visible light on phenylalanine molecules adsorbed in nanoparticles aggregates that generate an intense quadrupolar field.[47] This geometry complicates the interpretation of the signal because the molecular orientation is not guaranteed to be isotropic. The present simulations for randomly oriented sample show that the effect exists in solution and is a clear signature of molecular chirality.

■ ASSOCIATED CONTENT

Supporting Information

The Supporting Information is available free of charge on the ACS Publications website at DOI: 10.1021/acs.jctc.9b00346.

Derivations of the linear absorption in the minimal-coupling picture; details of the rotational averaging of the signals; CD, HD, and CHD signals for the beam waist w_0 = 15 nm; Figure S1, rotationally averaged signals for the beam waist w_0 = 15 nm; Figure S2, signal variations with the linear displacement for the beam waist w_0 = 15 nm; and Figure S3, translationally and rotationally averaged signals for the beam waist w_0 = 15 nm (PDF)

■ AUTHOR INFORMATION

Corresponding Authors

*E-mail: lyuzhouy@uci.edu.
*E-mail: smukamel@uci.edu.

ORCID

Shaul Mukamel: 0000-0002-6015-3135

Funding

This work was supported by the Chemical Sciences, Geosciences, and Biosciences Division, Office of Basic Energy Sciences, Office of Science, U.S. Department of Energy awards (DOE) DE-FG02-04ER15571 (J.R.R.) and DE-SC0019484 (L.Y.); and the National Science Foundation Grant CHE-1663822.

Notes

The authors declare no competing financial interest.

■ REFERENCES

(1) Aspinall, H. C. Chiral lanthanide complexes: coordination chemistry and applications. *Chem. Rev.* **2002**, *102*, 1807−1850.
(2) Štěpnička, P. Coordination and catalytic chemistry of phosphinoferrocene carboxamides. *Coord. Chem. Rev.* **2017**, *353*, 223−246.
(3) Singh, A.; Kumar Chopra, H. Chiral ionic liquids: design, synthesis and applications in asymmetric organo-catalysis. *Curr. Org. Synth.* **2017**, *14*, 488−510.
(4) Francotte, E.; Lindner, W. *Chirality in Drug Research*; Wiley-VCH: Weinheim, 2006.
(5) Patel, R. N. Biocatalysis for synthesis of pharmaceuticals. *Bioorg. Med. Chem.* **2018**, *26*, 1252−1274.
(6) Ojima, I. *Catalytic Asymmetric Synthesis*, 3rd ed.; John Wiley & Sons: New York, 2010.
(7) Rubin, N.; Perugia, E.; Goldschmidt, M.; Fridkin, M.; Addadi, L. Chirality of amyloid suprastructures. *J. Am. Chem. Soc.* **2008**, *130*, 4602−4603.
(8) Koga, N.; Tatsumi-Koga, R.; Liu, G.; Xiao, R.; Acton, T. B.; Montelione, G. T.; Baker, D. Principles for designing ideal protein structures. *Nature* **2012**, *491*, 222.
(9) Jurado, R.; Adamcik, J.; López-Haro, M.; González-Vera, J. A.; Ruiz-Arias, Á.; Sánchez-Ferrer, A.; Cuesta, R.; Domínguez-Vera, J. M.; Calvino, J. J.; Orte, A.; Mezzenga, R.; Gálvez, N. Apoferritin protein amyloid fibrils with tunable chirality and polymorphism. *J. Am. Chem. Soc.* **2019**, *141*, 1606−1613.
(10) Berova, N.; Nakanishi, K.; Woody, R. W. *Circular Dichroism: Principles and Applications*; John Wiley & Sons: New York, 2000.
(11) Kobayashi, N.; Muranaka, A. *Circular Dichroism and Magnetic Circular Dichroism Spectroscopy for Organic Chemists*; Royal Society of Chemistry: UK, 2012.
(12) Berova, N.; Polavarapu, P. L.; Nakanishi, K.; Woody, R. W. *Comprehensive Chiroptical Spectroscopy: Applications in Stereochemical Analysis of Synthetic Compounds, Natural Products, and Biomolecules*; John Wiley & Sons: New York, 2012; Vol. 2.
(13) Cornelis, D.; Franz, E.; Asselberghs, I.; Clays, K.; Verbiest, T.; Koeckelberghs, G. Interchromophoric interactions in chiral X-type π-conjugated oligomers: a linear and nonlinear optical study. *J. Am. Chem. Soc.* **2011**, *133*, 1317−1327.
(14) Monnaie, F.; Ceunen, W.; De Winter, J.; Gerbaux, P.; Cocchi, V.; Salatelli, E.; Koeckelberghs, G. Synthesis and transfer of chirality in supramolecular hydrogen bonded conjugated diblock copolymers. *Macromolecules* **2015**, *48*, 90−98.
(15) Tang, Y.; Cohen, A. E. Enhanced enantioselectivity in excitation of chiral molecules by superchiral light. *Science* **2011**, *332*, 333−336.
(16) Allen, L.; Beijersbergen, M. W.; Spreeuw, R.; Woerdman, J. Orbital angular momentum of light and the transformation of Laguerre-Gaussian laser modes. *Phys. Rev. A: At., Mol., Opt. Phys.* **1992**, *45*, 8185.
(17) Yao, A. M.; Padgett, M. J. Orbital angular momentum: origins, behavior and applications. *Adv. Opt. Photonics* **2011**, *3*, 161−204.
(18) Andrews, D. L.; Babiker, M. *The Angular Momentum of Light*; Cambridge University Press: New York, 2012.

DOI: 10.1021/acs.jctc.9b00346
J. Chem. Theory Comput. XXXX, XXX, XXX−XXX

(19) He, H.; Friese, M.; Heckenberg, N.; Rubinsztein-Dunlop, H. Direct observation of transfer of angular momentum to absorptive particles from a laser beam with a phase singularity. *Phys. Rev. Lett.* **1995**, *75*, 826.
(20) Grier, D. G. A revolution in optical manipulation. *Nature* **2003**, *424*, 810.
(21) Wang, X.-L.; Chen, J.; Li, Y.; Ding, J.; Guo, C.-S.; Wang, H.-T. Optical orbital angular momentum from the curl of polarization. *Phys. Rev. Lett.* **2010**, *105*, 253602.
(22) Padgett, M.; Bowman, R. Tweezers with a twist. *Nat. Photonics* **2011**, *5*, 343.
(23) Fürhapter, S.; Jesacher, A.; Bernet, S.; Ritsch-Marte, M. Spiral phase contrast imaging in microscopy. *Opt. Express* **2005**, *13*, 689−694.
(24) Altman, A. R.; Köprülü, K. G.; Corndorf, E.; Kumar, P.; Barbosa, G. A. Quantum imaging of nonlocal spatial correlations induced by orbital angular momentum. *Phys. Rev. Lett.* **2005**, *94*, 123601.
(25) Kolobov, M. I. *Quantum Imaging*; Springer Science & Business Media: New York, 2007.
(26) Boyer, V.; Marino, A.; Lett, P. Generation of spatially broadband twin beams for quantum imaging. *Phys. Rev. Lett.* **2008**, *100*, 143601.
(27) Mair, A.; Vaziri, A.; Weihs, G.; Zeilinger, A. Entanglement of the orbital angular momentum states of photons. *Nature* **2001**, *412*, 313.
(28) Barreiro, J. T.; Wei, T.-C.; Kwiat, P. G. Beating the channel capacity limit for linear photonic superdense coding. *Nat. Phys.* **2008**, *4*, 282.
(29) Nagali, E.; Sansoni, L.; Sciarrino, F.; De Martini, F.; Marrucci, L.; Piccirillo, B.; Karimi, E.; Santamato, E. Optimal quantum cloning of orbital angular momentum photon qubits through Hong−Ou−Mandel coalescence. *Nat. Photonics* **2009**, *3*, 720.
(30) Leach, J.; Jack, B.; Romero, J.; Jha, A. K.; Yao, A. M.; Franke-Arnold, S.; Ireland, D. G.; Boyd, R. W.; Barnett, S. M.; Padgett, M. J. Quantum correlations in optical angle−orbital angular momentum variables. *Science* **2010**, *329*, 662−665.
(31) Zhou, Z.-Y.; Li, Y.; Ding, D.-S.; Zhang, W.; Shi, S.; Shi, B.-S.; Guo, G.-C. Orbital angular momentum photonic quantum interface. *Light: Sci. Appl.* **2016**, *5*, No. e16019.
(32) Wang, X.-L.; Luo, Y.-H.; Huang, H.-L.; Chen, M.-C.; Su, Z.-E.; Liu, C.; Chen, C.; Li, W.; Fang, Y.-Q.; Jiang, X.; Zhang, J.; Li, L.; Liu, N.-L.; Lu, C.-Y.; Pan, J.-W. 18-Qubit entanglement with six photons' three degrees of freedom. *Phys. Rev. Lett.* **2018**, *120*, 260502.
(33) Géneaux, R.; Camper, A.; Auguste, T.; Gobert, O.; Caillat, J.; Taïeb, R.; Ruchon, T. Synthesis and characterization of attosecond light vortices in the extreme ultraviolet. *Nat. Commun.* **2016**, *7*, 12583.
(34) Rebernik Ribič, P. c. v.; Rösner, B.; Gauthier, D.; Allaria, E.; Döring, F.; Foglia, L.; Giannessi, L.; Mahne, N.; Manfredda, M.; Masciovecchio, C.; Mincigrucci, R.; Mirian, N.; Principi, E.; Roussel, E.; Simoncig, A.; Spampinati, S.; David, C.; De Ninno, G. Extreme-ultraviolet vortices from a free-electron laser. *Phys. Rev. X* **2017**, *7*, 031036.
(35) Denoeud, A.; Chopineau, L.; Leblanc, A.; Quéré, F. Interaction of ultraintense laser vortices with plasma mirrors. *Phys. Rev. Lett.* **2017**, *118*, 033902.
(36) Kong, F.; Zhang, C.; Bouchard, F.; Li, Z.; Brown, G. G.; Ko, D. H.; Hammond, T. J.; Arissian, L.; Boyd, R. W.; Karimi, E.; Corkum, P. B. Controlling the orbital angular momentum of high harmonic vortices. *Nat. Commun.* **2017**, *8*, 14970.
(37) Gauthier, D.; Ribič, P. R.; Adhikary, G.; Camper, A.; Chappuis, C.; Cucini, R.; DiMauro, L. F.; Dovillaire, G.; Frassetto, F.; Géneaux, R.; Miotti, P.; Poletto, L.; Ressel, B.; Spezzani, C.; Stupar, M.; Ruchon, T.; De Ninno, G. Tunable orbital angular momentum in high-harmonic generation. *Nat. Commun.* **2017**, *8*, 14971.
(38) Peele, A. G.; McMahon, P. J.; Paterson, D.; Tran, C. Q.; Mancuso, A. P.; Nugent, K. A.; Hayes, J. P.; Harvey, E.; Lai, B.; McNulty, I. Observation of an x-ray vortex. *Opt. Lett.* **2002**, *27*, 1752−1754.
(39) Peele, A. G.; Nugent, K. A.; Mancuso, A. P.; Paterson, D.; McNulty, I.; Hayes, J. P. X-ray phase vortices: theory and experiment. *J. Opt. Soc. Am. A* **2004**, *21*, 1575−1584.
(40) Xie, C.; Zhu, X.; Shi, L.; Liu, M. Spiral photon sieves apodized by digital prolate spheroidal window for the generation of hard-x-ray vortex. *Opt. Lett.* **2010**, *35*, 1765−1767.
(41) Hemsing, E.; Marinelli, A. Echo-enabled X-ray vortex generation. *Phys. Rev. Lett.* **2012**, *109*, 224801.
(42) Ribič, P. R.; Gauthier, D.; De Ninno, G. Generation of coherent extreme-ultraviolet radiation carrying orbital angular momentum. *Phys. Rev. Lett.* **2014**, *112*, 203602.
(43) Vila-Comamala, J.; Sakdinawat, A.; Guizar-Sicairos, M. Characterization of x-ray phase vortices by ptychographic coherent diffractive imaging. *Opt. Lett.* **2014**, *39*, 5281−5284.
(44) Rosenzweig, J. B. Twisted light beyond the visible. *Nat. Photonics* **2019**, *13*, 141−143.
(45) Lee, J. C. T.; Alexander, S. J.; Kevan, S. D.; Roy, S.; McMorran, B. J. Laguerre-Gauss and Hermite-Gauss soft X-ray states generated using diffractive optics. *Nat. Photonics* **2019**, *13*, 205−209.
(46) Taira, Y.; Kohmura, Y. Measuring the topological charge of an x-ray vortex using a triangular aperture. *J. Opt.* **2019**, *21*, 045604.
(47) Brullot, W.; Vanbel, M. K.; Swusten, T.; Verbiest, T. Resolving enantiomers using the optical angular momentum of twisted light. *Sci. Adv.* **2016**, *2*, No. e1501349.
(48) Forbes, K. A.; Andrews, D. L. Optical orbital angular momentum: twisted light and chirality. *Opt. Lett.* **2018**, *43*, 435−438.
(49) Babiker, M.; Bennett, C.; Andrews, D.; Romero, L. D. Orbital angular momentum exchange in the interaction of twisted light with molecules. *Phys. Rev. Lett.* **2002**, *89*, 143601.
(50) Andrews, D. L.; Romero, L. D.; Babiker, M. On optical vortex interactions with chiral matter. *Opt. Commun.* **2004**, *237*, 133−139.
(51) Araoka, F.; Verbiest, T.; Clays, K.; Persoons, A. Interactions of twisted light with chiral molecules: An experimental investigation. *Phys. Rev. A: At., Mol., Opt. Phys.* **2005**, *71*, 055401.
(52) Löffler, W.; Broer, D.; Woerdman, J. Circular dichroism of cholesteric polymers and the orbital angular momentum of light. *Phys. Rev. A: At., Mol., Opt. Phys.* **2011**, *83*, 065801.
(53) Giammanco, F.; Perona, A.; Marsili, P.; Conti, F.; Fidecaro, F.; Gozzini, S.; Lucchesini, A. Influence of the photon orbital angular momentum on electric dipole transitions: negative experimental evidence. *Opt. Lett.* **2017**, *42*, 219−222.
(54) Tanaka, S.; Chernyak, V.; Mukamel, S. Time-resolved X-ray spectroscopies: Nonlinear response functions and Liouville-space pathways. *Phys. Rev. A: At., Mol., Opt. Phys.* **2001**, *63*, 063405.
(55) Chernyak, V. Y.; Saurabh, P.; Mukamel, S. Non-linear non-local molecular electrodynamics with nano-optical fields. *J. Chem. Phys.* **2015**, *143*, 164107.
(56) Rouxel, J. R.; Kowalewski, M.; Mukamel, S. Current vs charge density contributions to nonlinear X-ray spectroscopy. *J. Chem. Theory Comput.* **2016**, *12*, 3959−3968.
(57) Kerber, R. M.; Fitzgerald, J. M.; Oh, S. S.; Reiter, D. E.; Hess, O. Orbital angular momentum dichroism in nanoantennas. *Commun. Phys.* **2018**, *1*, 87.
(58) Werner, H.-J.; Knowles, P.; Knizia, G.; Manby, F. R.; Schütz, M.; Celani, P.; Korona, T.; Lindh, R.; Mitrushenkov, A.; Rauhut, G.; Shamasundar, K. R.; Adler, T. B.; Amos, R. D.; Bernhardsson, A.; Berning, A.; Cooper, D. L.; Deegan, M. J. O.; Dobbyn, A. J.; Eckert, F.; Goll, E.; Hampel, C.; Hesselmann, A.; Hetzer, G.; Hrenar, T.; Jansen, G.; Köppl, C.; Liu, Y.; Lloyd, A. W.; Mata, R. A.; May, A. J.; McNicholas, S. J.; Meyer, W.; Mura, M. E.; Nicklass, A.; O'Neill, D. P.; Palmieri, P.; Pflüger, K.; Pitzer, R.; Reiher, M.; Shiozaki, T.; Stoll, H.; Stone, A. J.; Tarroni, R.; Thorsteinsson, T.; Wang, M.; Wolf, A. *MOLPRO, version 2010.1, a package of ab initio programs*; 2010; see http://www.molpro.net.
(59) Douglas, M.; Kroll, N. M. Quantum electrodynamical corrections to the fine structure of helium. *Ann. Phys.* **1974**, *82*, 89−155.

DOI: 10.1021/acs.jctc.9b00346
J. Chem. Theory Comput. XXXX, XXX, XXX−XXX

(60) Hess, B. A. Relativistic electronic-structure calculations employing a two-component no-pair formalism with external-field projection operators. *Phys. Rev. A: At., Mol., Opt. Phys.* **1986**, *33*, 3742.
(61) Dunning, T. H., Jr Gaussian basis sets for use in correlated molecular calculations. I. The atoms boron through neon and hydrogen. *J. Chem. Phys.* **1989**, *90*, 1007−1023.
(62) Werner, H.-J.; Meyer, W. A quadratically convergent multiconfiguration−self-consistent field method with simultaneous optimization of orbitals and CI coefficients. *J. Chem. Phys.* **1980**, *73*, 2342−2356.
(63) Werner, H.-J.; Knowles, P. J. A second order multiconfiguration SCF procedure with optimum convergence. *J. Chem. Phys.* **1985**, *82*, 5053−5063.
(64) Knowles, P. J.; Werner, H.-J. An efficient second-order MC SCF method for long configuration expansions. *Chem. Phys. Lett.* **1985**, *115*, 259−267.
(65) Rompel, A.; Cinco, R. M.; Latimer, M. J.; McDermott, A. E.; Guiles, R.; Quintanilha, A.; Krauss, R. M.; Sauer, K.; Yachandra, V. K.; Klein, M. P. Sulfur K-edge X-ray absorption spectroscopy: a spectroscopic tool to examine the redox state of S-containing metabolites in vivo. *Proc. Natl. Acad. Sci. U. S. A.* **1998**, *95*, 6122−6127.
(66) Mimura, H.; Handa, S.; Kimura, T.; Yumoto, H.; Yamakawa, D.; Yokoyama, H.; Matsuyama, S.; Inagaki, K.; Yamamura, K.; Sano, Y.; Tamasaku, K.; Nishino, Y.; Yabashi, M.; Ishikawa, T.; Yamauchi, K. Breaking the 10 nm barrier in hard-X-ray focusing. *Nat. Phys.* **2010**, *6*, 122.
(67) Pikuz, T.; Faenov, A.; Matsuoka, T.; Matsuyama, S.; Yamauchi, K.; Ozaki, N.; Albertazzi, B.; Inubushi, Y.; Yabashi, M.; Tono, K.; Sato, Y.; Yumoto, H.; Ohashi, H.; Pikuz, S.; Grum-Grzhimailo, A. N.; Nishikino, M.; Kawachi, T.; Ishikawa, T.; Kodama, R. 3D visualization of XFEL beam focusing properties using LiF crystal X-ray detector. *Sci. Rep.* **2016**, *5*, 17713.
(68) Ribič, P. R.; Rösner, B.; Gauthier, D.; Döring, F.; Masciovecchio, C.; Principi, E.; David, C.; De Ninno, G. Extreme-Ultraviolet Vortices at a Free-Electron Laser. *Microsc. Microanal.* **2018**, *24*, 296−297.

DOI: 10.1021/acs.jctc.9b00346
J. Chem. Theory Comput. XXXX, XXX, XXX−XXX

SUPPORTING INFORMATION

Probing molecular chirality by orbital angular momentum carrying X-ray pulses

Lyuzhou Ye,[*,†] Jérémy R. Rouxel,[‡,¶] Shahaf Asban,[†] Benedikt Rösner,[¶] and Shaul Mukamel[*,†]

†*Department of Chemistry and Department of Physics and Astronomy, University of California, Irvine, CA 92697, USA*

‡*Laboratory of Ultrafast Spectroscopy, École Polytechnique Fédérale de Lausanne, CH-1015 Lausanne, Switzerland*

¶*Paul Scherrer Institut, 5232 Villigen PSI, Switzerland*

E-mail: lyuzhouy@uci.edu; smukamel@uci.edu

S1 Linear absorption in the minimal-coupling representation

The absorption of an incoming light field is self-heterodyne detected, which is defined as the time-integrated rate-of-change of the photon number

$$S(t) = \int_0^t dt' \left\langle \frac{dN}{dt'} \right\rangle \tag{S1}$$

$$= -\frac{1}{\hbar} \int d\boldsymbol{r} \int_0^t dt' \, \boldsymbol{J}(\boldsymbol{r}, t') \cdot \boldsymbol{A}(\boldsymbol{r}, t'), \tag{S2}$$

where the gauge-invariant current density is

$$\boldsymbol{J}(\boldsymbol{r},t') = \langle\langle \hat{\boldsymbol{J}}(\boldsymbol{r},t')|\rho(t')\rangle\rangle = \mathrm{Tr}\left[\hat{\boldsymbol{J}}(\boldsymbol{r},t')\exp_+\left(-i\int H_{\mathrm{int},-}(t')\right)\rho_{\mathrm{eq}}\right], \tag{S3}$$

with $\hat{\boldsymbol{J}} = \hat{\boldsymbol{j}} - \frac{e}{mc}\hat{\sigma}\boldsymbol{A}$. $H_{\mathrm{int},-}$ is the Liouville space superoperator, with its action on a Hilbert space operator as $H_{\mathrm{int},-}O = H_{\mathrm{int}}O - OH_{\mathrm{int}}$.

By expanding the exponential in Eq. S3 perturbatively in $H_{\mathrm{int},-}$, and collecting the terms n-th ordered in $\boldsymbol{A}$, we can obtain the n-th order nonlocal response function. Hereafter we consider the linear ($n = 1$) response function. The contributing terms are

$$-\frac{e}{mc}\langle\langle\hat{\sigma}(\boldsymbol{r},t)|\rho_{\mathrm{eq}}\rangle\rangle, \tag{S4}$$

and

$$\frac{i}{\hbar}\int d\boldsymbol{r}'\int_{-\infty}^{t} dt'\langle\langle\hat{\boldsymbol{j}}(\boldsymbol{r},t)|\boldsymbol{j}_-(\boldsymbol{r}',t')|\rho_{\mathrm{eq}}\rangle\rangle. \tag{S5}$$

The linear current density is then given by

$$\boldsymbol{J}_x(\boldsymbol{r},t) = \sum_{x'}\int d\boldsymbol{r}'\int_{-\infty}^{t} dt'\,\zeta_{x,x'}(\boldsymbol{r}t;\boldsymbol{r}'t')\boldsymbol{A}_{x'}(\boldsymbol{r}',t'), \tag{S6}$$

with the nonlocal linear response function being

$$\zeta_{x,x'}(\boldsymbol{r},t;\boldsymbol{r}',t') = \frac{i}{\hbar}\langle[\hat{\boldsymbol{j}}_x(\boldsymbol{r},t),\hat{\boldsymbol{j}}_{x'}(\boldsymbol{r}',t')]\rangle - \frac{e}{mc}\langle\hat{\sigma}(\boldsymbol{r},t)\rangle\delta(\boldsymbol{r}-\boldsymbol{r}')\delta(t-t')\delta_{x,x'}. \tag{S7}$$

Assuming that the system is initially in the ground state $|g\rangle$, we have

$$\langle[\hat{\boldsymbol{j}}_x(\boldsymbol{r},t),\hat{\boldsymbol{j}}_{x'}(\boldsymbol{r}',t)]\rangle = 2i\Im\left[\sum_c \boldsymbol{j}_{x,gc}(\boldsymbol{r})\boldsymbol{j}_{x',cg}(\boldsymbol{r}')e^{-i\omega_{cg}(t-t')}\right]. \tag{S8}$$

Substituting Eqs. S6 and S8 into Eq. S2 and neglecting the off-resonant term (i.e. $\sigma\boldsymbol{A}^2$), we

have the sum-over-states expression for the linear absorption signal in time domain

$$S_{\mathrm{abs}}(t) = -\frac{2}{\hbar^2}\mathrm{Im}\sum_c \int d\boldsymbol{r}d\boldsymbol{r}' \Big[\boldsymbol{j}_{gc}(\boldsymbol{r})\cdot\boldsymbol{A}(\boldsymbol{r})\boldsymbol{j}_{cg}(\boldsymbol{r}')\cdot\boldsymbol{A}(\boldsymbol{r}')e^{-i\omega_{cg}t} - \boldsymbol{j}_{cg}(\boldsymbol{r})\cdot\boldsymbol{A}(\boldsymbol{r})\boldsymbol{j}_{gc}(\boldsymbol{r}')\cdot\boldsymbol{A}(\boldsymbol{r}')e^{-i\omega_{cg}t}\Big]. \tag{S9}$$

The frequency domain signal is

$$S_{\mathrm{abs}}(\omega) = -\frac{2}{\hbar^2}\mathrm{Im}\sum_c \left[\frac{\int d\boldsymbol{r}\,\boldsymbol{j}_{gc}(\boldsymbol{r})\cdot\boldsymbol{A}(\boldsymbol{r})\int d\boldsymbol{r}'\,\boldsymbol{j}_{cg}(\boldsymbol{r}')\cdot\boldsymbol{A}(\boldsymbol{r}')}{\omega-\omega_{gc}+i\Gamma_{gc}} - \frac{\int d\boldsymbol{r}\,\boldsymbol{j}_{cg}(\boldsymbol{r})\cdot\boldsymbol{A}(\boldsymbol{r})\int d\boldsymbol{r}'\,\boldsymbol{j}_{gc}(\boldsymbol{r}')\cdot\boldsymbol{A}(\boldsymbol{r}')}{\omega-\omega_{cg}+i\Gamma_{cg}}\right]. \tag{S10}$$

This gives the absorption signal of oriented molecules. The CD, HD and CHD signals in the main text can be obtained by performing the rotational averaging on Eq. S26. Details are given in Sec. S3.

S2 Expanding the Laguerre-Gauss modes the Hermite-Gaussian basis

For the X-ray circular dichroism, we choose the beam waist $w_0 = 60\,\mathrm{nm}$, the wavelength $\lambda = 0.5\,\mathrm{nm}$. The Rayleigh length is $z_R = \pi\frac{w_0^2}{\lambda} = 22.6\,\mu\mathrm{m}$, which is much larger than the size of a molecule. We can therefore make the following approximations:

$$R(z) \to \infty, \tag{S11}$$

$$w(z) = w_0, \tag{S12}$$

$$\exp\left(-ik\frac{r^2}{2R(z)}\right) = 1, \tag{S13}$$

$$\phi_{lp}(z) = 0. \tag{S14}$$

The Laguerre-Gauss beam can be simplified to the form

$$\mathrm{LG}_{lp}(r,\phi)=\sqrt{\frac{2p!}{\pi(p+|l|)!}}\exp\left(-\frac{r^2}{w_0^2}\right)\left(\frac{\sqrt{2}r}{w_0}\right)^{|l|}L_p^{|l|}\left(\frac{2r^2}{w_0^2}\right)e^{il\phi}. \tag{S15}$$

Using the method in Ref ,[1] we can expand the generalized Laguerre polynomial ($l\geq 0$) in the Hermite-Gaussian basis as

$$L_p^l(r^2)=\frac{(-i)^l r^{-l}e^{r^2}e^{-il\phi}}{\pi p!}\frac{\pi}{(-2i)^{2p+l}e^{r^2}}\sum_{u=0}^{p}\sum_{v=0}^{l}\binom{p}{u}\binom{l}{v}i^v H_{2u+l-v}(x)H_{2p-2u+v}(y), \tag{S16}$$

where $H_n(x)$ is the Hermite polynomial. We rearrange Eq. S16 as

$$r^l e^{il\phi}L_p^l(r^2)=\frac{(-1)^p}{2^{2p+l}p!}\sum_{u=0}^{p}\sum_{v=0}^{l}\binom{p}{u}\binom{l}{v}i^v H_{2u+l-v}(x)H_{2p-2u+v}(y). \tag{S17}$$

The real part of the above equation is

$$C_{lp}(x,y)\equiv\cos(l\phi)r^l L_p^l(r^2) \tag{S18}$$

$$=\frac{(-1)^p}{2^{2p+l}p!}\sum_{u=0}^{p}\sum_{v=0}^{[l/2]}\binom{p}{u}\binom{l}{2v}(-1)^v H_{2u+l-2v}(x)H_{2p-2u+2v}(y), \tag{S19}$$

and the imaginary part is

$$S_{lp}(x,y)\equiv\sin(l\phi)r^l L_p^l(r^2) \tag{S20}$$

$$=\frac{(-1)^p}{2^{2p+l}p!}\sum_{u=0}^{p}\sum_{v=0}^{[(l-1)/2]}\binom{p}{u}\binom{l}{2v+1}(-1)^v H_{2u+l-2v-1}(x)H_{2p-2u+2v+1}(y). \tag{S21}$$

The LG mode in Hermite-Gaussian basis reads, for $l\geq 0$,

$$\mathrm{LG}_{lp}(x,y)=\sqrt{\frac{2p!}{\pi(p+|l|)!}}\exp\left(-\frac{x^2+y^2}{w_0^2}\right)\left[C_{lp}\left(\frac{\sqrt{2}x}{w_0},\frac{\sqrt{2}y}{w_0}\right)+iS_{lp}\left(\frac{\sqrt{2}x}{w_0},\frac{\sqrt{2}y}{w_0}\right)\right], \tag{S22}$$

and for $l < 0$,

$$\mathrm{LG}_{lp}(x,y) = \sqrt{\frac{2p!}{\pi(p+|l|)!}} \exp\left(-\frac{x^2+y^2}{w_0^2}\right) \left[C_{|l|p}\left(\frac{\sqrt{2}x}{w_0}, \frac{\sqrt{2}y}{w_0}\right) - iS_{|l|p}\left(\frac{\sqrt{2}x}{w_0}, \frac{\sqrt{2}y}{w_0}\right)\right]. \tag{S23}$$

S3 Rotationally-averaged signals

In the ZXZ convention, the rotation matrix is

$$\boldsymbol{R}(\alpha,\beta,\gamma) = \begin{pmatrix} \cos\alpha\cos\gamma - \cos\beta\sin\alpha\sin\gamma & -\cos\alpha\sin\gamma - \cos\beta\cos\gamma\sin\alpha & \sin\alpha\sin\beta \\ \cos\gamma\sin\alpha + \cos\alpha\cos\beta\sin\gamma & \cos\alpha\cos\beta\cos\gamma - \sin\alpha\sin\gamma & -\cos\alpha\sin\beta \\ \sin\beta\sin\gamma & \cos\gamma\sin\beta & \cos\beta \end{pmatrix}, \tag{S24}$$

with the Euler angles $\alpha \in [0, 2\pi]$, $\beta \in [0, \pi]$, and $\gamma \in [0, 2\pi]$.

The current density $\boldsymbol{j}(\boldsymbol{r})$ is expanded over the Gaussian type orbitals

$$\boldsymbol{j}(\boldsymbol{r}) = \sum_i c_i g_i(\boldsymbol{r}; a_i, b_i, c_i, \boldsymbol{r}_{pi}, \alpha_{pi}) = \sum_i c_i (x - x_{pi})^{a_i} (y - y_{pi})^{b_i} (z - z_{pi})^{c_i} e^{-\alpha_{pi}(\boldsymbol{r}-\boldsymbol{r}_{pi})^2}. \tag{S25}$$

To perform the rotational averaging, we rotate the molecule by the angle (α, β, γ), and the corresponding absorption signal is

$$S_{\mathrm{abs}}(\omega,\alpha,\beta,\gamma) = -\frac{2}{\hbar^2}\mathrm{Im}\sum_c \left[\frac{\int d\boldsymbol{r}\, \boldsymbol{R}\boldsymbol{j}_{gc}(\boldsymbol{R}^{-1}\boldsymbol{r}) \cdot \boldsymbol{A}(\boldsymbol{r}) \int d\boldsymbol{r}'\, \boldsymbol{R}\boldsymbol{j}_{cg}(\boldsymbol{R}^{-1}\boldsymbol{r}') \cdot \boldsymbol{A}(\boldsymbol{r}')}{\omega - \omega_{gc} + i\Gamma_{gc}} \right.$$
$$\left. - \frac{\int d\boldsymbol{r}\, \boldsymbol{R}\boldsymbol{j}_{cg}(\boldsymbol{R}^{-1}\boldsymbol{r}) \cdot \boldsymbol{A}(\boldsymbol{r}) \int d\boldsymbol{r}'\, \boldsymbol{R}\boldsymbol{j}_{gc}(\boldsymbol{R}^{-1}\boldsymbol{r}') \cdot \boldsymbol{A}(\boldsymbol{r}')}{\omega - \omega_{cg} + i\Gamma_{cg}} \right]. \tag{S26}$$

Referring to Eqs. S22, S23 and S25, we then need to evaluate the integral of the following

form

$$I(\alpha,\beta,\gamma)=\int d\boldsymbol{r}\; g(\boldsymbol{R}^{-1}\boldsymbol{r};a,b,c,\boldsymbol{r}_p,\alpha_p)\exp\left(-\frac{x^2+y^2}{w_0^2}\right)H_m\left(\frac{\sqrt{2}x}{w_0}\right)H_n\left(\frac{\sqrt{2}y}{w_0}\right)e^{-ik_0z}. \tag{S27}$$

The final expression for $I(\alpha,\beta,\gamma)$ reads

$$\begin{aligned}
I(\alpha,\beta,\gamma)=&\sum_{r=0}^{[m/2]}\sum_{0\le s+t\le m-2r}\sum_{r'=0}^{[n/2]}\sum_{0\le s'+t'\le n-2r'}(-1)^{r+r'}\frac{m!c_x^s c_y^t c_z^{m-2r-s-t}2^{m-2r}}{r!s!t!(m-2r-s-t)!}\frac{n!b_x^{s'}b_y^{t'}b_z^{n-2r'-s'-t'}2^{n-2r'}}{r'!s'!t'!(n-2r'-s'-t')!}\\
&\times\sum_{d=0}^{a}\sum_{f=0}^{[(d+s+s')/2]}\sum_{0\le g+h\le d+s+s'-2f}\frac{a!}{d!(a-d)!}\frac{(d+s+s')!}{f!g!h!(d+s+s'-2f-g-h)!}\sqrt{\frac{\pi}{\alpha_p+c_{xx}}}\\
&\times\frac{(-x_p)^{a-d}e^{-\alpha_p x_p^2}2^{d+s+s'-2f}}{[4(\alpha_p+c_{xx})]^{d+s+s'-f}}(2\alpha_p x_p-i\sin\alpha\sin\beta k_0)^g e^{\frac{(2\alpha_p x_p-i\sin\alpha\sin\beta k_0)^2}{4(\alpha_p+c_{xx})}}(-c_{xy})^h(-c_{zx})^{d+s+s'-2f-g}\\
&\times\sum_{d'=0}^{b}\sum_{f'=0}^{[(t+t'+d'+h)/2]}\sum_{g'=0}^{t+t'+d'+h-2f'}e^{-\alpha_p y_p^2}\sqrt{\frac{\pi}{A}}\frac{b!}{d'!(b-d')!}\frac{(t+t'+d'+h)!}{f'!g'!(t+t'+d'+h-2f'-g')!}\\
&\times\frac{(-y_p)^{b-d'}2^{t+t'+d'+h-2f'}}{(4A)^{t+t'+d'+h-f'}}e^{\frac{B^2}{4A}}B^{g'}C^{t+t'+d'+h-2f'-g'}\\
&\times\sum_{d''=0}^{c}\sum_{f''=0}^{[(m-2r+n-2r'+d''+d-2f-g+d'-2f'-g')/2]}\frac{(2F)^{m-2r+n-2r'+d''+d-2f-g+d'-2f'-g'-2f''}}{(4D)^{m-2r+n-2r'+d''+d-2f-g+d'-2f'-g'-f''}}\\
&\times\sqrt{\frac{\pi}{D}}e^{-\alpha_p z_p^2}\frac{c!(-z_p)^{c-d''}}{d''!(c-d'')!}e^{\frac{F^2}{4D}}\frac{(m-2r+n-2r'+d''+d-2f-g+d'-2f'-g')!}{f''!(m-2r+n-2r'+d''+d-2f-g+d'-2f'-g'-2f'')!},
\end{aligned} \tag{S28}$$

where the relevant parameters are

$$b_x = \frac{\sqrt{2}(-\cos\beta\cos\gamma\sin\alpha - \cos\alpha\sin\gamma)}{w_0}, \tag{S29}$$

$$b_y = \frac{\sqrt{2}(\cos\alpha\cos\beta\cos\gamma - \sin\alpha\sin\gamma)}{w_0}, \tag{S30}$$

$$b_z = \frac{\sqrt{2}\cos\gamma\sin\beta}{w_0}, \tag{S31}$$

$$c_x = \frac{\sqrt{2}(\cos\alpha\cos\gamma - \cos\beta\sin\alpha\sin\gamma)}{w_0}, \tag{S32}$$

$$c_y = \frac{\sqrt{2}(\cos\gamma\sin\alpha + \cos\alpha\cos\beta\sin\gamma)}{w_0}, \tag{S33}$$

$$c_z = \frac{\sqrt{2}\sin\beta\sin\gamma}{w_0}, \tag{S34}$$

$$c_{xx} = \frac{\cos^2\alpha + \cos^2\beta\sin^2\alpha}{w_0^2}, \tag{S35}$$

$$c_{yy} = \frac{\cos^2\alpha\cos^2\beta + \sin^2\alpha}{w_0^2}, \tag{S36}$$

$$c_{zz} = \frac{\sin^2\beta}{w_0^2}, \tag{S37}$$

$$c_{xy} = \frac{2\sin\alpha\cos\alpha\sin^2\beta}{w_0^2}, \tag{S38}$$

$$c_{yz} = \frac{2\cos\alpha\sin\beta\cos\beta}{w_0^2}, \tag{S39}$$

$$c_{zx} = \frac{-2\cos\beta\sin\alpha\sin\beta}{w_0^2}, \tag{S40}$$

$$A = \alpha_p + c_{yy} - \frac{c_{xy}^2}{4(\alpha_p + c_{xx})}, \tag{S41}$$

$$B = 2\alpha_p y_p + i\cos\alpha\sin\beta k_0 - \frac{(2\alpha_p x_p - i\sin\alpha\sin\beta k_0)c_{xy}}{2(\alpha_p + c_{xx})}, \tag{S42}$$

$$C = \frac{c_{xy}c_{zx}}{2(\alpha_p + c_{xx})} - c_{yz}, \tag{S43}$$

$$D = \alpha_p + c_{zz} - \frac{c_{zx}^2}{4(\alpha_p + c_{xx})} - \frac{C^2}{4A}, \tag{S44}$$

$$F = 2\alpha_p z_p - \frac{(2\alpha_p x_p - i\sin\alpha\sin\beta k_0)c_{zx}}{2(\alpha_p + c_{xx})} + \frac{BC}{2A} - i\cos\beta k_0. \tag{S45}$$

The rotationally-averaged signal can be calculated as

$$S_{\rm abs}(\omega) = \int_0^{2\pi} d\alpha \int_0^{\pi} \sin\beta d\beta \int_0^{2\pi} d\gamma \, S_{\rm abs}(\omega, \alpha, \beta, \gamma). \tag{S46}$$

S4 Signals with the $w_0 = 15\,\mathrm{nm}$ beam waist

Here, we show the CD, HD and CHD signals with the beam waist $w_0 = 15\,\mathrm{nm}$, which corresponds to the current technological limit.[2,3] We can see that similar results, as those in the main text with the beam waist $w_0 = 60\,\mathrm{nm}$, are observed in Figs. S1, S2 and S3. This is because the beam waist is much larger than the size of molecule, and thus the signals are not quite sensitive to the size of beam waist. This makes the measurement of HD and CHD signals feasible even with a relatively large beam waist in the X-ray in experiment.

References

(1) Kimel, I.; Elias, L. R. Relations between hermite and laguerre gaussian modes. *IEEE Journal of quantum electronics* **1993**, *29*, 2562–2567.

(2) others,, et al. Breaking the 10 nm barrier in hard-X-ray focusing. *Nature physics* **2010**, *6*, 122.

(3) others,, et al. 3D visualization of XFEL beam focusing properties using LiF crystal X-ray detector. *Scientific reports* **2015**, *5*, 17713.

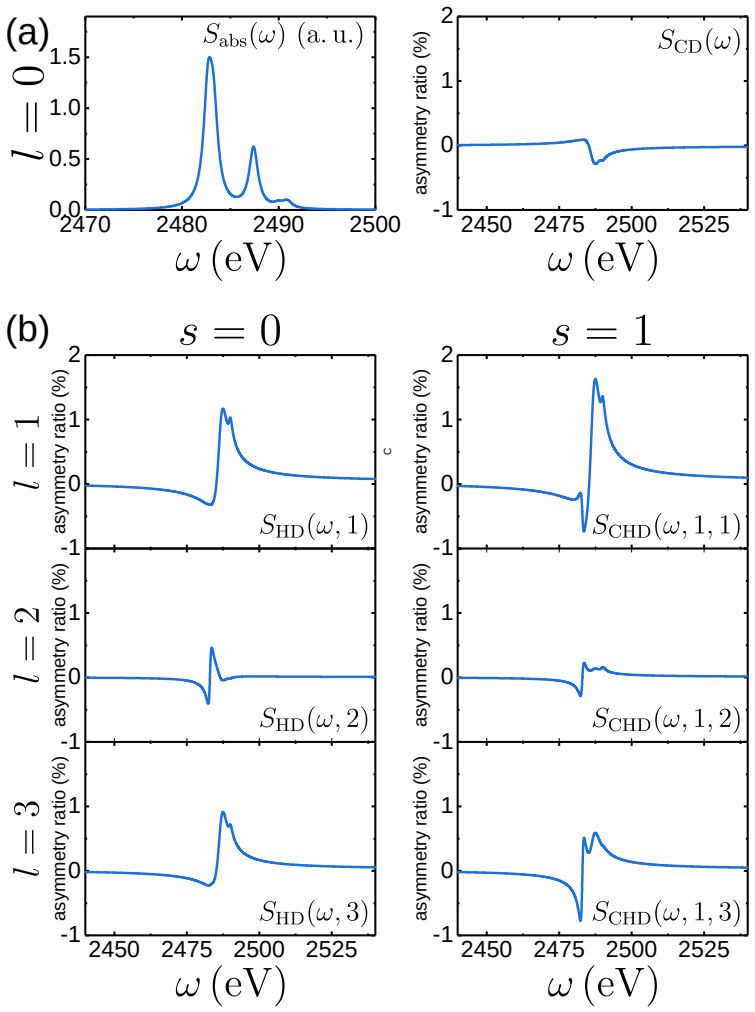

Fig. S 1: The same as Fig. 2 of the main text, except that the beam waist $w_0 = 15\,\text{nm}$.

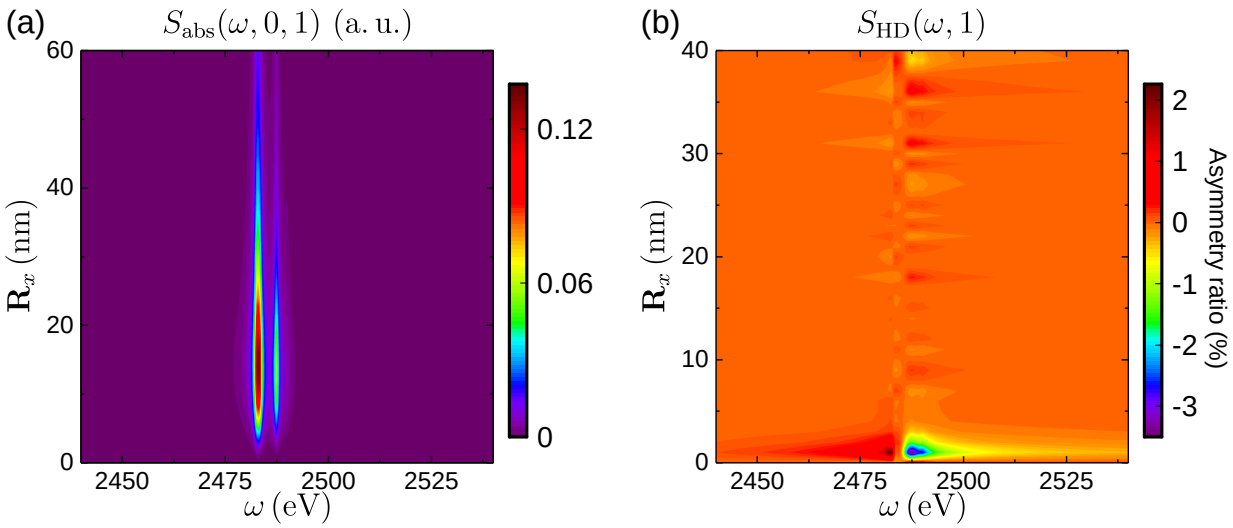

Fig. S 2: The same as Fig. 3 of the main text, except that the beam waist $w_0 = 15\,\text{nm}$.

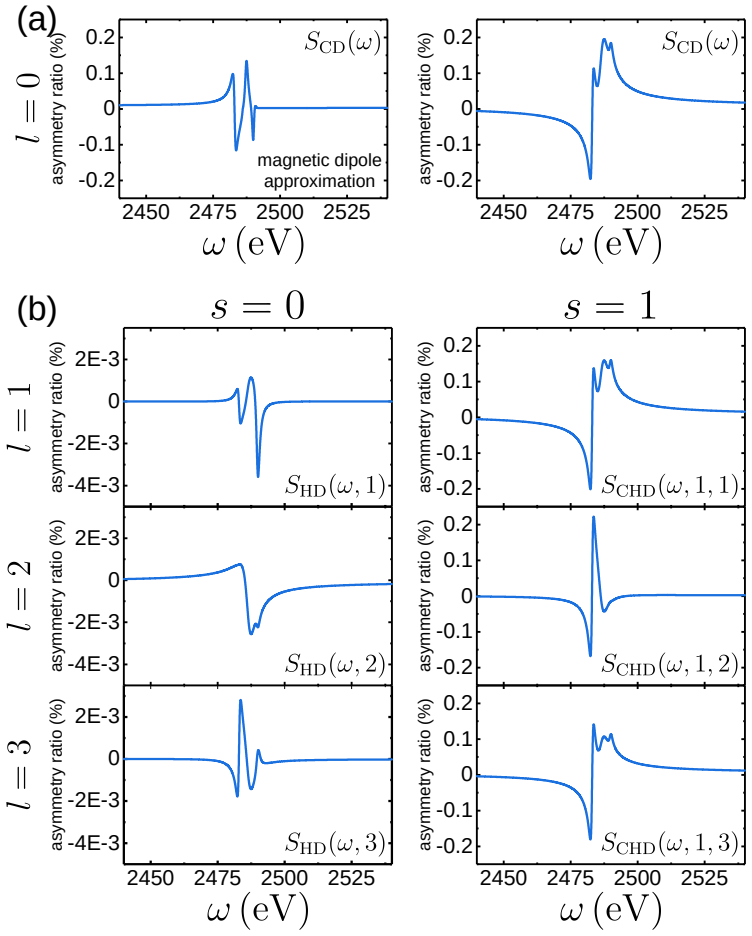

Fig. S 3: The same as Fig. 4 of the main text, except that the beam waist $w_0 = 15\,\mathrm{nm}$.